TUTORIAL REVIEW

Check for updates

Waste-derived green N-doped materials: mechanistic insights, synthesis, and comprehensive evaluation

Xiang-Mao Huang, Mengyao Gao,* Dessie Ashagrie Tafere, Shao-Yu Wang, Luthfiyyah Annisa Nur Azizah and Yan-Ling Yang

Nitrogen (N)-doped materials derived from biomass hold great promise for energy storage, gas adsorption, catalysis, and water treatment, offering an effective strategy for waste valorization. Precise control over temperature and nitrogen doping levels has been shown to enhance the surface area and multifunctional properties. This review begins by covering fundamental principles such as band gap and electronegativity, followed by an analysis of N-doping preparation methods, focusing on pyridinic N, graphitic N, and oxidized N and their applications, especially in energy storage, carbon dioxide (CO_2) capture, and as catalysts for hydrogen generation. Additionally, density functional theory (DFT) calculations are carried out to elucidate the structural and electrochemical properties of N-doped materials. This review seeks to advance the sustainable development of waste-derived green materials by conducting a comprehensive comparative analysis of material activation and carbonization mechanisms. Furthermore, it addresses the challenges, perspectives, and prospects of waste valorisation for green N-doped materials, exploring their potential across diverse applications.

Sustainability spotlight

Nitrogen doping modifies the electronic structure, band gap, and surface chemistry of materials, improving performance sustainably. By controlling the temperature and doping levels, the surface area and multifunctional properties are optimized, enhancing applications in eco-friendly energy storage, catalysis, and gas adsorption. This process reduces waste generation, aligning with green chemistry principles for a more sustainable future. This review discusses green synthesis methods for various N-doping configurations (pyridinic, graphitic, and oxidized N) to promote material sustainability. It highlights eco-friendly activation and carbonization processes that improve the structural integrity and electrochemical performance, all the while minimizing the environmental footprint. This section uses density functional theory (DFT) to predict and validate the properties of N-doped materials derived from waste, supporting sustainable practices. It assesses the challenges, potential improvements, and future opportunities for applying these green materials in energy storage, gas adsorption, catalysis, and water treatment, contributing to a circular economy and promoting environmental sustainability.

1. Introduction

Our planet is undergoing a rapid energy crisis, accompanied by floods, wildfires, and extreme heat waves. A green reset must be prioritized to place sustainable development at the forefront. This shift is crucial for scientists to effectively address the urgent energy and environmental challenges we now face.[1] In response to the high demand for renewable resources, various types of biomass wastes have gained significant attention as precursors for nitrogen-doped (N-doped) materials.[2] These include animal-derived wastes, such as fish bone,[3] shrimp shell,[4,5] chicken feather,[6] animal manure[7–9] and animal collagen,[10] and plant-based wastes, including orange peel,[11] tamarind shell,[12] algae,[13] sugarcane bagasse,[14] soybean seeds[15]

and sunflower seeds.[16] These biomass resources offer a promising route for the synthesis of N-doped carbon materials, due to their low cost, wide availability, and rich composition of heteroatoms such as O, N, and S, as well as trace metals.[15–18]

Green chemistry is associated with the design of chemical products and processes that minimize the use and generation of hazardous substances.[19–23] In this context, it is important to highlight the role of activated carbon derived from lignocellulosic biomass, which includes carbon materials obtained from grass, wood, corn stalk, and other crop residues. These carbon materials exhibit excellent electrical conductivity, a well-developed porous structure, and high specific surface area, thereby facilitating efficient charge transport and providing ample space for ion storage.[24]

Due to the unique combination of renewability, low cost, natural abundance, sustainability, and microstructural tunability, biomass-derived carbon materials have been widely applied in various fields,[16–18] including air pollution control,[25]

Department of Chemical Engineering, National Taiwan University of Science and Technology, Taipei 10607, Taiwan. E-mail: mygao@mail.ntust.edu.tw

water desalination, wastewater treatment,[26] supercapacitors,[27] greenhouse gas emissions,[28] membrane technology, electrochemistry,[18] and energy storage.[26,29] Resources such as the biomass (lignocellulose),[30–33] wood biomass[34] and agricultural residues/by products have been considered as main materials for the N-doping applications.[35–39] In particular, waste-derived biomass, such as coconut shells,[25] cotton-based,[40] sugarcane-based,[41] macroalgae,[13] water hyacinth and water lettuce,[33] has shown great potential as precursors for activated carbon, suitable not only for energy storage but also for various environmental and catalytic applications.

Biomass has emerged as a sustainable source for green carbon materials through processes involving nitrogen incorporation, pre-carbonization, and activation, which enhance the surface area and introduce key functional groups.[42] Fig. 1 schematically presents these steps, emphasizing the structural evolution of biomass into functionalized carbon. Nitrogen atoms play a pivotal role in modifying the structure,[16,43–46] morphology[16,43–46] and electrochemical properties[47–49] of carbon materials. Activated carbon could be considered a candidate for the excellent high storage performance of N atoms, where these materials are doped into the structure of materials and present on the surface of materials. They can form functional groups, such as amine ($-NH_2$) and nitroso ($-NO$). Furthermore, nitrogen atoms can be incorporated directly into the carbon lattice in several forms such as pyridinic-N, pyrrolic-N, graphitic-N, oxidized-N, and graphite-N,[27] each contributing distinct electronic and catalytic properties. Nitrogen-doped carbon derived from biomass demonstrates remarkable potential in a range of applications. In this review, we focus particularly on its utility in energy storage systems, carbon dioxide (CO_2) capture, and as a catalyst for hydrogen evolution reactions.

To obtain N-doped materials, various processes have been developed, including pre-carbonization, carbonization, and activation (either physical or chemical). Pre-carbonization is the initial phase of carbonization, during which organic or polymeric precursors undergo partial thermal decomposition. In this stage, the material is subjected to moderate temperatures ranging from 200 to 400 °C. Carbonization is the process of converting organic materials into carbon or carbon-rich residues through pyrolysis. Activation, whether physical or chemical, enhances the surface area and porosity of the carbonized materials. This step often facilitates the preparation of the material for subsequent high-temperature carbonization by stabilizing its structure.[25] The type and distribution of nitrogen functionalities, previously discussed, are strongly influenced by these processing conditions. Specifically, the carbonization temperature, nitrogen precursors, and activation method govern the incorporation of nitrogen into the carbon matrix, impacting both the structural and electronic characteristics of

Green materials	Seeds of sunflower	Corncob	Coconut Shell
Introducing nitrogen atoms	NH_3	NH_3	Ammoxidation
Pre-carbonization, carbonization and	Precarbonization: 12 h Carbonization: 2 h Activation 500 °C at 2 h Activation 800 °C in 1 h	400–800 °C	Ammoxidation at 350 °C for 5 h. Carbonization in 500 °C
Specific surface areas (SSA)	453 m² g⁻¹	1154 m² g⁻¹	1037 to 2995 m² g⁻¹
Functional groups	C=C, C=O Types of the nitrogen	C–O, C=O and –OH, Ph–NH₂ and pyridine-N	N–H stretching, N–H deformation, and C–N stretching vibrations pyridinic-N (N-6), pyrrolic-/pyridonic-N (N–5), and quaternary-N (N–Q), N–H stretching, N–H deformation, and C–N

Fig. 1 Illustration depicting plants as a precursor for green materials, showcasing the introduction of nitrogen atoms, pre-carbonization and activation processes, enhancement of specific surface area, and incorporation of functional groups for improved functionality.

Table 1 Advantages and disadvantages of different precursors in the activation of materials

Activator	Advantages	Disadvantages	References
NH_3	Higher material density, cost-effective, environmental friendliness, and high material density	Lower surface area	50
CO_2	Activation occurs at the solid–gas interface, CO_2 generates large micro- and mesopores, and increases the catalytic activity	Leads to incomplete N-doping	51
KOH	High performance, high specific surface area, hierarchical porous structures, effective migration channels for the electrolytic ions, leading to high rate performances, and generates high nanopores	Low material density, corrosion behavior, not environmentally friendly, KOH requires relatively high temperature (>600 °C), and corrosive	15 and 52–55
K_2FeO_4	Powerful oxidizing agent *via* different pH, environmentally friendly oxidant, improve magnetization and pore size, lower temperatures	Unstable and restrict scale application and development in industrial large applications	56–60
$ZnCl_2$	Improve the carbon content, lower yield, prevents hyperactivation, better control on porosity, and more micropores	Problem with dosage, expensive, improper tuned pore structure and surface properties	61–63
H_3PO_4	Cost-effective, less corrosive, a suitable crosslinking and dehydrating agent, and low toxicity	Depends on impregnation solution because of high polar characteristic	64–66
Na_2CO_3	Depends on the temperature, optimal performance, and high surface area	Microporous solids and a relatively small external area	67 and 68

the final material. A summary of common activation agents and their respective advantages and limitations is presented in Table 1.

This review provides an in-depth overview of the synthesis methods for various waste-derived N-doped materials, with an emphasis on environmentally friendly and sustainable production strategies.[25,50,61] We explore green activation approaches, structural evolution during thermal processing, and the resulting physicochemical properties of N-doped carbon. The mechanisms governing nitrogen doping efficiency and the impact of process variables are critically examined. Additionally, we discuss post-synthesis modifications and evaluate the performance of these materials in applications such as adsorption, catalysis, membrane separation, and electrochemical energy storage. Finally, the review concludes with a forward-looking perspective on future challenges and opportunities for the large-scale implementation of green, waste-derived N-doped materials in circular technologies.

2. Principles for enhancing the sustainable approach toward waste valorization

2.1. Band gap

The relationship between band gap engineering and nitrogen-doped carbon materials is central to their performance in

energy conversion and storage applications. The band gap is defined as the energy difference between the valence band and conduction band, which determines a material's ability to conduct electricity.[69] Nitrogen doping introduces new electronic states within the carbon lattice, effectively narrowing the band gap and enabling easier electron transitions. This facilitates enhanced charge transport, improving the material's conductivity and reactivity. The type (*e.g.*, pyridinic, graphitic, and oxidized) and concentration of nitrogen dopants strongly influence the extent of band gap reduction and the formation of localized states. These modifications directly affect the material's optical and electronic behavior, making N-doped carbon highly suitable for photocatalysis, electrocatalysis, and electrochemical energy storage (*e.g.*, batteries and supercapacitors). Fig. 2a demonstrates this concept by comparing materials with no band gap, a small band gap, and a large band gap, illustrating how smaller gaps correlate with higher conductivity due to facilitated electron transition.

2.2. Electronegativity

Electronegativity, the tendency of an atom to attract electrons in a chemical bond, plays a key role in the charge redistribution in N-doped carbon materials.[70] Nitrogen, with a higher electronegativity (3.04) than carbon (2.55), draws electron density towards itself when doped into a carbon matrix, resulting in localized dipoles and a shift in electron density away from adjacent carbon atoms. This polarization effect, visualized in
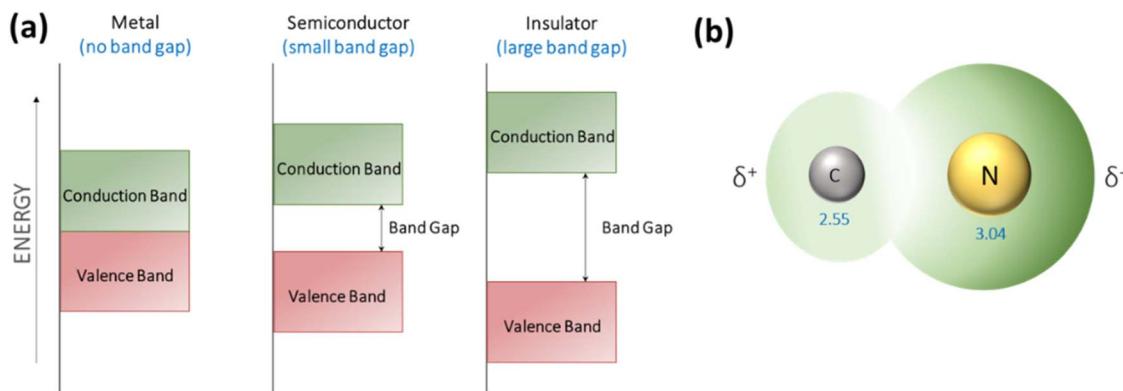
Fig. 2 Schematic representation of (a) the effect of band gap size on electronic conductivity, showing materials with no band gap, small band gap, and large band gap. Smaller band gaps enable easier electron transition and higher conductivity. (b) Electronegativity difference between nitrogen (N) and carbon (C), illustrating charge redistribution due to N-doping. Nitrogen's higher electronegativity leads to electron accumulation (δ^-) around N and depletion (δ^+) around adjacent carbon atoms, enhancing the material's reactivity and electronic properties.

Fig. 2b, leads to charge accumulation around nitrogen (δ^-) and depletion near carbon atoms (δ^+). Such asymmetry modifies the electronic structure, contributes to band gap narrowing, and enhances electrical conductivity.[71] This redistribution of charge not only improves electron mobility but also activates new reactive sites, especially relevant in oxygen reduction reactions (ORRs) and other catalytic pathways. In energy storage systems, this altered charge landscape promotes efficient ion adsorption and fast electron transfer, enhancing both the capacity and rate performance. From a theoretical perspective, electronegativity is not directly measurable as an energy value but is inferred based on ionization energy, electron affinity, and atom size. It generally increases across a period and decreases down a group. For instance, nonmetals such as O_2 and N_2, with high electronegativity, tend to attract shared electrons more strongly in covalent bonds. When electrons are shared unequally, as is the case in N-doped carbons, the stronger pull of nitrogen results in electron density distortion that affects the geometry and reactivity. This charge imbalance leads to structural relaxation and formation of localized electronic states, further validating the role of electronegativity in improving the catalytic efficiency and electronic conductivity in green N-doped materials.

2.3. Electrical conductivity

Electrical conductivity is a critical parameter in evaluating the electronic behavior of materials, especially semiconductors and carbon-based nanostructures such as single-walled carbon nanotubes (SWCNTs).[72] The conductivity of semiconductor materials depends on the concentration of charge carriers. At elevated temperatures (e.g., 410–450 K), semiconductors exhibit intrinsic conductivity, wherein electrons at the top of the valence band are thermally excited to the conduction band, leaving behind holes.[73] Each excited electron creates a corresponding hole, resulting in equal concentrations of electrons and holes. The carrier concentration (N_i) in such intrinsic semiconductors can be expressed using classical Boltzmann statistics.[74]

$$N_i = N = P = ZT^{\frac{3}{2}} \exp\left(-\frac{E_g}{2kT}\right) \tag{1}$$

where Z is a constant, T is the thermodynamic temperature, k is the Boltzmann constant, and E_g is the band gap width of the semiconductor. The carrier concentration (N_i) of the semiconductor material at elevated temperatures demonstrates a direct proportionality to the cube root of temperature.

The intrinsic conductivity of the high-temperature conducting region can be formulated as follows:

$$\sigma = Z \exp\left(-\frac{E_g}{2kT}\right) \tag{2}$$

After applying the logarithmic transformation to eqn (2), the slope of the resulting line can be determined via fitting curve analysis, allowing for the expression of the band gap width:

$$E_g = -2k\Delta T \ln \sigma \tag{3}$$

The electrical conductivity was determined by obtaining the $I–V$ curve at different doping concentrations and different temperatures. The conductivity formula is described as follows.

$$\sigma = \frac{I \times L}{V \times A} \tag{4}$$

where I is the electric current, V is the applied voltage, L is the average length of the SWCNTs, and A is the average cross-sectional area obtained from transmission electron microscopy (TEM) characterization. The enhanced conductivity in N-doped carbon materials is primarily attributed to charge redistribution driven by electronegativity differences, which alters the band structure and improves charge mobility. As a result, these materials demonstrate excellent potential in applications such as electrocatalysis, batteries, supercapacitors, and photocatalysis, where efficient electron transfer is essential.

3. Different N-doping types based on carbonization temperatures

Carbonization temperature plays a critical role in determining the porosity, elemental composition, and nitrogen

Table 2 Elemental composition and C/O molar ratios of N-doped carbon at various carbonization temperatures

Carbonization temperature/°C	N (%)	C (%)	S (%)	O (%)	C/O molar ratio
600	6.54	74.80	0.22	18.94	5.26
650	4.25	76.38	0.20	16.25	6.26
700	3.31	76.73	0.19	18.88	5.42
750	2.32	80.81	0.16	16.15	6.67
800	2.48	78.09	0.45	17.47	5.96
850	1.14	84.96	0.16	13.38	8.47
900	1.05	84.61	0.21	13.31	8.49
950	0.92	88.19	0.23	10.08	11.67

configuration of biomass-derived N-doped carbon materials. These materials typically exhibit a hierarchical porous structure, consisting of micropores (<2 nm), mesopores (2–50 nm), and macropores (>50 nm),[75] which is essential for optimizing ion diffusion, mass transport, and surface reactivity in electrochemical systems.

As the carbonization temperature increases from 600 °C to 950 °C, a significant transformation in chemical composition is observed. Specifically, the nitrogen content decreases from 6.54% to 0.92%, while the carbon content increases from 74.80% to 88.19% and the oxygen content decreases from 18.94% to 10.08%. This shift reflects enhanced thermal decomposition, deoxygenation, and graphitic ordering within

the carbon matrix. The C/O molar ratio, which reflects the material's reduction capacity and degree of graphitization, correspondingly increases with temperature, peaking at 11.67 at 950 °C (Table 2).

The evolution of nitrogen bonding environments with temperature was investigated using X-ray photoelectron spectroscopy (XPS). At 600 °C, the N 1s spectrum exhibits peaks corresponding to pyrrolic-N (∼400.0 eV) and pyridinic-N (∼400.4 eV). As temperature increases, pyridinic-N decreases significantly, and quaternary-N (graphitic-N) emerges, indicating ring-opening reactions and nitrogen rearrangement. Between 750 °C and 950 °C, both quaternary-N and pyrrolic-N contents gradually decline due to thermal decomposition. The order of thermal stability is: quaternary-N > pyrrolic-N > pyridinic-N, highlighting the prevalence of graphitic nitrogen at higher temperatures.

Fig. 3a clearly shows this spectral evolution: pyridinic- and pyrrolic-N dominate at lower temperatures, while quaternary-N intensifies at elevated temperatures. Fig. 3b outlines the bonding configurations of each nitrogen type: pyridinic-N at graphene edges, pyrrolic-N within five-membered rings, and quaternary-N replacing a carbon atom in the graphitic plane. Fig. 3c summarizes the thermally induced transitions, emphasizing how increasing temperature promotes the conversion of labile nitrogen species into more stable graphitic configurations.

These nitrogen types directly influence electrochemical behaviour. Pyridinic-N, bonded to two carbon atoms, donates
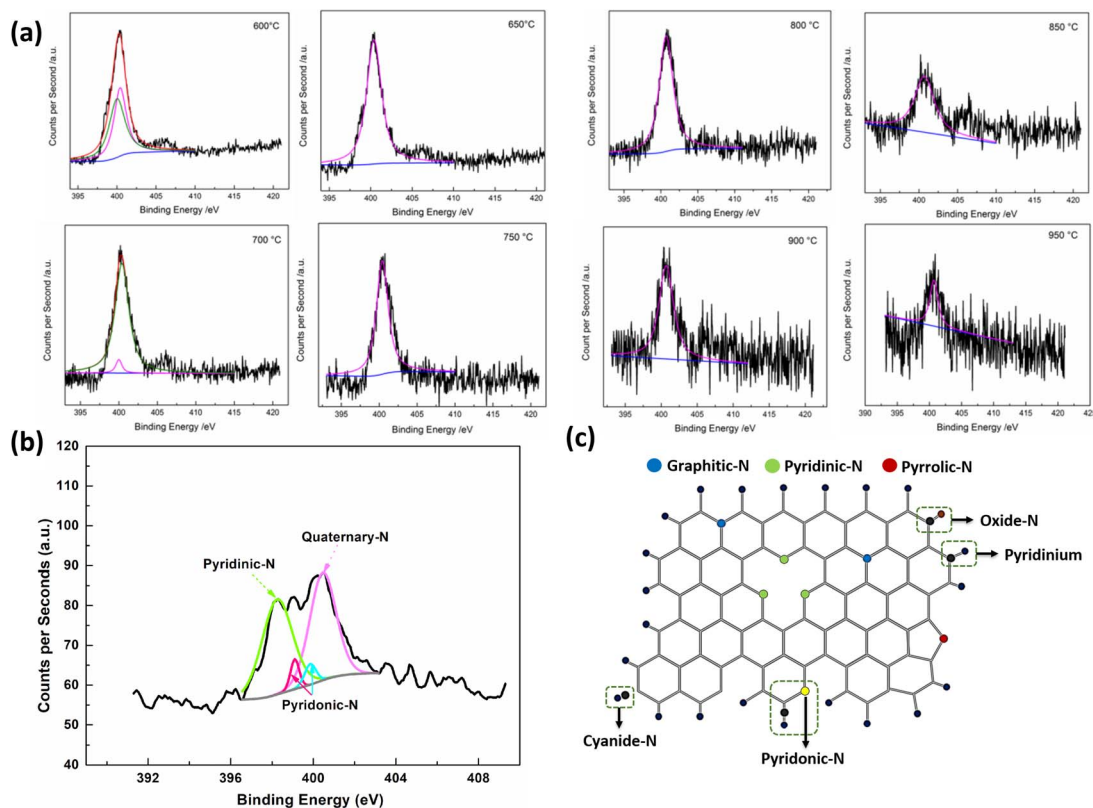

Fig. 3 (a) High-resolution N 1s XPS spectra of carbonized materials at various temperatures, showing the transformation of pyridinic- and pyrrolic-N into quaternary-N. (b) Bonding configurations and relative thermal stabilities of pyridinic-N, pyrrolic-N, and graphitic-N. (c) Schematic illustration of nitrogen species transformation pathways during thermal treatment. Adapted from ref. 76.

one p-electron to the π-system, facilitating charge delocalization and catalysis (*e.g.*, ORR). Pyrrolic-N, part of a five-membered ring, donates two p-electrons and contributes to redox processes. Quaternary-N, embedded within the graphitic framework, improves the conductivity and structural integrity, essential for applications in oxygen reduction, oxygen evolution, and supercapacitor systems.[77,78] Notably, pyrrolic-N is gradually converted into graphitic-N at temperatures above 800 °C, further enhancing the electrical performance and stability of the material.

Complementary XPS analysis of C 1s and O 1s spectra confirms the presence of functional groups such as C–C, C–O, C–N, O=C, O–C, and O–N, which evolve with temperature and influence the surface reactivity.[14,15,17] These bonding states are quantitatively determined using the electron binding energy equation:
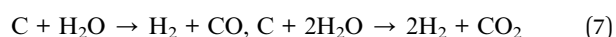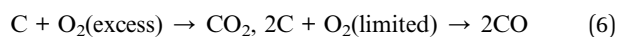
$$E_{binding} = E_{photon} - (E_{kinetic} + \phi) \tag{5}$$

where $E_{binding}$ is the binding energy (BE) of the electron measured relative to the chemical potential, E_{photon} is the energy of the X-ray photons being used, $E_{kinetic}$ is the kinetic energy of the electron as measured by the instrument and ϕ is a work function-like term for the specific surface of the material, which in real measurements includes a small correction by the instrument's work function because of the contact potential.

4. Effect of activation on the hierarchical porous structure

In the preparation of porous carbon materials using activation methods, the raw materials are typically subjected to a pre-carbonization treatment known as the carbonization process. The main objective is to eliminate volatile components from the organic matter and increase the carbon content, forming an initial pore structure suitable for subsequent activation. The carbonization temperature is generally determined based on thermogravimetric analysis (TGA). Parameters such as heating rate, gas flow rate, and carbonization time influence the physicochemical properties of the resulting carbon. Excessively high carbonization temperatures produce dense structures with low porosity, hindering activation, while low temperatures yield porous but mechanically weak precursors.[79] Thus, optimized carbonization conditions tailored to the feedstock are essential.
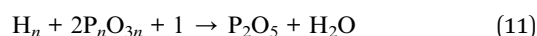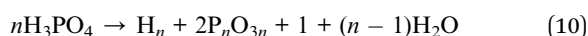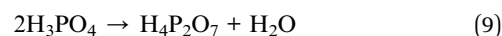
Physical activation involves heating the carbonized material at high temperatures using oxidizing gases such as steam, CO_2, O_2, and air to develop a porous structure within the pyrolysis product.[80] During activation, the primary process involves selective chemical reactions between the activation gas and the carbon atoms on the material's surface, forming volatile gases that etch the material and create pores. The specific reactions are described as follows:

$$C + O_2(excess) \rightarrow CO_2, 2C + O_2(limited) \rightarrow 2CO \tag{6}$$

$$C + H_2O \rightarrow H_2 + CO, C + 2H_2O \rightarrow 2H_2 + CO_2 \tag{7}$$

$$C + CO_2 \rightarrow 2CO \tag{8}$$

The temperature for physical activation is generally controlled within the range of 800–1000 °C. If the activation temperature is too low, the prepared porous carbon material will have a low specific surface area and an underdeveloped pore structure. Conversely, if the activation temperature is too high, it will result in excessive carbon loss, affecting the yield. While this method introduces no impurities and avoids environmental contamination, it is energy-intensive.

Chemical activation involves impregnating the precursor raw material with chemical activators, followed by carbonization and activation in an inert gas medium. Common activators include alkaline activators (KOH and NaOH), acidic activators (H_3PO_4 and H_2SO_4), and salts ($ZnCl_2$, K_2CO_3, and Na_2CO_3).[81] In China, the most common method for producing activated carbon is using $ZnCl_2$ activation. During activation, $ZnCl_2$ has a strong dehydrating effect, causing the H and O elements in the raw material to be removed as $H_2O(g)$, forming a developed porous structure. In contrast, using H_3PO_4 as an activator has the advantage of a lower activation temperature, typically between 300 and 350 °C, resulting in porous carbon materials with rich mesoporous structures. This method is also cost-effective, less toxic, and widely adopted in the United States. Currently, KOH is the most commonly used activator for preparing high-performance porous carbon materials. Using KOH as an activator often results in porous carbon materials with a high specific surface area and a well-developed microporous structure. Additionally, the pore size of the prepared porous carbon materials can be controlled by adjusting the amount of KOH used.
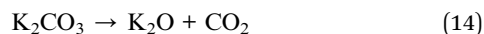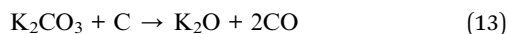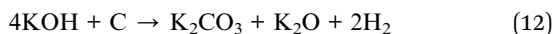
During the carbonization process, $ZnCl_2$, with a low melting point (238 °C), penetrates the precursor material *in situ*, serving as a template to generate interconnected pores. Simultaneously, the activation effect of $ZnCl_2$ reduces the oxygen content and enhances the electrical conductivity. In phosphate activation, at 400 °C, P-species doping induces lattice distortion or expands the (002) plane spacing, while partial oxidation of carbonaceous organics forms P–O–C structures. Phosphate and polyphosphate species form *via* interactions between H_3PO_4 and the organic matrix, attaching to cross-linked polymer fragments and exposing phosphate peaks, including PO_2 and HPO_3. With further temperature increases, H_3PO_4 undergoes condensation and dehydration, converting into pyrophosphoric acid ($H_4P_2O_7$), polyphosphate ($H_{n+2}P_nO_{3n+1}$), and eventually phosphorus pentoxide (P_2O_5). P_2O_5 strongly oxidizes organic components, potentially degrading micropores.

$$2H_3PO_4 \rightarrow H_4P_2O_7 + H_2O \tag{9}$$

$$nH_3PO_4 \rightarrow H_n + 2P_nO_{3n} + 1 + (n-1)H_2O \tag{10}$$

$$H_n + 2P_nO_{3n} + 1 \rightarrow P_2O_5 + H_2O \tag{11}$$

For the KOH activation mechanism, it is relatively well established. The specific reactions are shown in equations. Compared to physical activation, chemical activation occurs at lower temperatures and produces porous carbon materials with

higher specific surface areas and more controllable pore structures. However, the corrosive nature of acidic or alkaline activators imposes stricter requirements on production equipment.

$$4KOH + C \rightarrow K_2CO_3 + K_2O + 2H_2 \tag{12}$$

$$K_2CO_3 + C \rightarrow K_2O + 2CO \tag{13}$$

$$K_2CO_3 \rightarrow K_2O + CO_2 \tag{14}$$

$$K_2O + C \rightarrow 2K + 2CO \tag{15}$$

The chemical physical activation method combines chemical activation and physical activation. Typically, the raw materials are first mixed with chemical activators, and then oxidizing gases (*i.e.*, oxygen, steam, or CO_2) are introduced and heated simultaneously. This hybrid method enhances reactivity and pore formation, resulting in porous carbon materials with a high specific surface area and abundant mesoporosity. Additionally, this method can introduce functional groups onto the carbon surface, imparting special properties for targeted applications.

N-doping methods significantly increase the number of electroactive sites, improving the catalytic and electronic properties of carbon materials.[82–91] The addition of N_2 (ref. 92) and hydrogen bonding[93] enhances surface polarity and electrostatic interactions,[92] thus modifying the structure. This section describes the N-doping process, starting from carbonization followed by activation of waste-based biomass, ultimately yielding nitrogen-doped porous carbon. From this perspective, sustainable valorization of waste materials can be successfully achieved. Generally, biomass-derived porous carbon can be applied in energy storage,[24] CO_2 capture,[94] and catalysis,[95] as shown in Fig. 4.

X-ray photoelectron spectroscopy (XPS) is recommended to evaluate the effects of processing temperature on nitrogen bonding and to locate specific nitrogen configurations such as pyridinic-N, quaternary-N, and graphitic-N. The advantages of chemical activation include high porosity,[25] large surface area and microporosity,[27] rapid processing, high carbon yield, energy efficiency, shorter soaking times, and lower operating temperatures.[96,97] In general, chemical activation facilitates hydrolysis.[97] On the other hand, it is associated with environmental impact,[25] higher temperature requirements, extended reaction time, and increased equipment demands.[98]

5. Methods of nitrogen-doping porous carbon: activation, carbonation, and post-treatment

The incorporation of nitrogen into porous carbon frameworks significantly modifies the surface chemistry, enhances porosity, and improves electrochemical properties, making it a pivotal strategy for advancing biomass-derived carbon materials.[42,94]
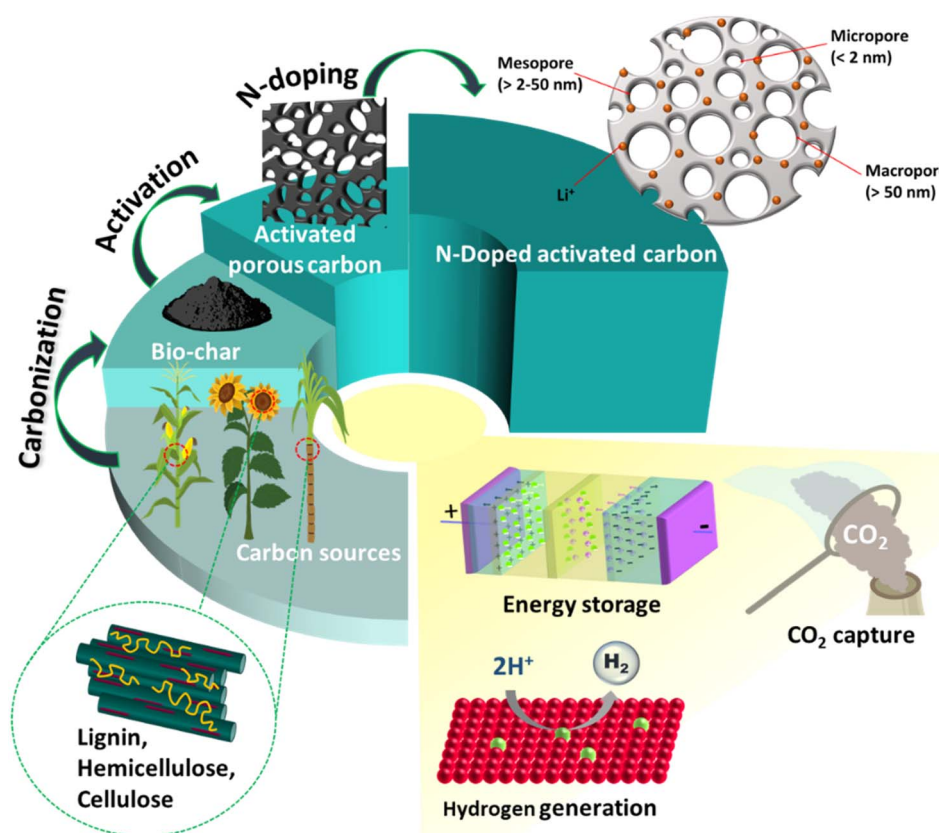

Fig. 4 Waste-derived carbon materials with porous structures and nitrogen doping, formed through carbonization and activation. These features enhance the interaction between water and the material surface, enabling applications in energy storage, CO_2 capture, and hydrogen evolution.

Functional groups such as carbonyl (C=O), hydroxyl (–OH), and carboxyl (–COOH) serve as key indicators of successful surface modification.[99] The dissociation of C–O and C–N bonds is facilitated by p–π conjugation and the presence of low-basicity heterocyclic nitrogen species (*e.g.*, pyrrole and pyridine). When embedded in a hydrogen-rich matrix, nitrogen-containing sites promote the binding of hydrogen radicals, boost redox activity, and redistribute electron density across the carbon skeleton. Thus, N-doping becomes a strategic tool to tailor electronic properties and enhance functionality in applications like energy storage, catalysis, and adsorption.

5.1. Nitrogen doping through carbonization of biomass-derived materials

Extensive research has focused on the synthesis of N-doped materials, namely using NH_3, ammoxidation, and urea, followed by chemical activation with potassium hydroxide (KOH) in order to obtain activated carbon from biomass for various applications and with unique structures.[12,14,16,17,40,100,101] KOH facilitates effective processing by enhancing specific surface area[54] and porous texture.[102]

Table 3 presents the comparison of nitrogen doping synthesis using NH_3, ammoxidation and urea with KOH chemical activation for carbonization of biomass-derived materials. For instance, ref. 40 used NH_3 for synthesizing cotton to generate cotton-based carbon fibers (CCFs) with turbostatic carbon and then activated with KOH. Carbonization was conducted in a conventional tube furnace, where the temperature was controlled at 700, 800, and 900 °C for 2 h, and the heating rate and flow rate of N_2 gas were set at 5 °C min^{-1} and 100 mL min^{-1}, respectively. The high specific surface area of the product at different temperatures of 700, 800, and 900 °C was 318.20, 602.10, and 778.60 m^2 g^{-1}, respectively. From this point of view, the higher temperature results in a larger surface area of 778.60 m^2 g^{-1} and a high mesopore composition of the material.[103] According to ref. 104, this material can be considered in the supercapacitor application. It is supported by the finding that electrical conductivity with a value of 0.04 S cm^2 can be obtained at a temperature of 900 °C. In this concept, higher carbonization temperature increases the conductivity in terms of preparation and carbonization of CCFs in NH_3. In contrast, higher carbonization temperature decreases the size of micropores during carbonization, and it can be found that carbonization at 800 °C shows a greater size compared to 900 °C with a value more than 3 nm, as observed from the peak evaluation.[40] Moreover, XPS analysis confirms that the content of O increases from 8.52 to 10.50% after CCF carbonization with N_2. Because of the presence of O 1s, it is clear that the O element exists in the material. It is also supported by the presence of C=O, C–O–C, C–O–H, and COOH in the material. In more detail, existence of a C=O functional group plays a major role in the electrochemical capacitance associated with the faradaic reaction[105,106] because of the redox reaction of N_2-based O_2 groups, where O_2 functional groups play a major role as electron acceptors[107] and N_2 plays an integral role as electron donors.[108] Also, part of C–OH groups are converted to C=O, confirming the increase of

C=O bonds.[105] Thus, it can be understood that the higher temperature of synthesized material improves the electrochemical capacitance because of the presence of O in C=O in the materials.

Gao *et al.* synthesized the activated carbon from licorice root residues derived from nitrogen doped porous carbon (NP-LRC).[17] One gram of licorice root powder was mixed with NH_4Cl and 1 g of KOH. Thereafter, a tube furnace was used for heating the materials, and carbon materials were dried in a vacuum oven at 60 °C for 12 h, and carbonization of materials was performed at 750 °C for 2 h. NP-LRC shows the surface area with a value of 1257.80 m^2 g^{-1}, with the pore size ranging from 2 to 5 nm, indicating the superior mesoporous structures. Also, the larger specific surface area and mesopores increases the permeation of electrolyte penetration and ion adsorption. According to ref. 111, the presence of O and N heteroatoms leads to a more efficient redox reaction. Binding energies are associated with the C (C 1s) atoms that are connected to an O (O 1s) atom with a single bond or to two O atoms.[55] Thus, the existence of O and N in the sample confirms the successful synthesis of materials.

An ammoxidation process is performed by mixing NH_3 with the material to create an activated carbon.[100] The coconut shell *via* the oxygen peroxide was then subject to the ammoxidation process and treated with KOH for activation for synthesizing the nitrogen-doped porous carbon. Carbonization was performed with a nitrogen flow rate of 200 mL min^{-1} and heating at 500 °C with a heating rate of 5 °C min^{-1}. Ammoxidation was conducted with a mixture of ammonia (NH_3) and air at a ratio of 1 : 10. Carbonization was conducted at 500 °C for 2 h. After that, it was cooled in a N_2 atmosphere. Furthermore, ammoxidation was performed at 350 °C for 5 h. Results indicated that the surface area was obtained in the range 1037–2995 m^2 g^{-1}. Also, the average pore diameters of micropores increased from 0.6 to 0.7 nm. Functional groups, namely, N–H and C–N, are found after activation. Moreover, N species found were pyridinic (N-6), pyrrolic/pyridinic (N-5) and quaternary-N (N-Q).

Many scholars used carbonization of urea for biomass synthesis, then activated *via* KOH to derive activated carbon from sugarcane bagasse,[14] tamarind shell,[12] macroalgae,[13] orange peel[11] and *Enteromorpha clathrata*.[110] Urea has been known for its non-toxicity, inexpensiveness and environmental friendliness.[112]. Ref. 14 synthesized a sugarcane-based material from sugarcane basse—5 g of sugarcane bagasse, urea (5 g) and KOH (5 g) were mixed in 100 mL deionized water and kept for 2 h. The precursor mixture was dried at 60 °C and then heated at 800 °C. The as-prepared sugarcane-based material had a specific surface area of 2905.4 m^2 g^{-1}. In this process, urea interacts with –OH and –COOH from cellulose and lignin to form H_2 bonds. Furthermore, the C 1s peak refers to the presence of functional groups, namely, C=O, C–C, C–O, and C–N. Then, the O 1s peak indicates the presence of O in the material as O–N, O=C, and O–C. Lastly, N 1s refers to pyridinic-N (N-6), pyrrolic N (N-5), quaternary N (N-Q) and oxidized N_2 atoms (N-X). Furthermore, ref. 110 assessed the activated carbon derived from *Enteromorpha clathrata*, synthesized using urea and activated with KOH in a tubular furnace. Then, the temperature was

Table 3 Nitrogen doping through carbonization of biomass-derived materials

Nitrogen doping	Green materials	Synthesis methods	Carbonization (°C)	Surface area (m² g⁻¹)	Functional groups	Ref.
NH$_3$	Cotton	Pre-carbonization: N/A Carbonization: 2 h Activation: N/A	N/A 700, 800, and 900 N/A	318.2–778.6	C=O, C–O–C, C–O–H, and COOH	40
NH$_3$	Licorice root	Pre-carbonization: N/A Carbonization: 2 h Activation: N/A	60 750 N/A	392.9–1257.8	O=C, C–O/C–OH and C–OOH	17
NH$_3$	Seeds of sunflower	Pre-carbonization: 12 h Carbonization: 2 h Activation: 2 h	N/A N/A 500 and 800	453.0	C=C and C=O	16
NH$_3$	Soybean	Pre-carbonization: N/A Carbonization: 2 h Activation: N/A	N/A 800 °C N/A	392.9–1257.8	O=C, C–O/C–OH and C–OOH	15
NH$_3$	Corncob	Pre-carbonization: N/A Carbonization: 2 h Activation: N/A	N/A 400–800 N/A	1154.0	C–O, C=O and –OH; Ph–NH$_2$ and pyridinic-N	109
Ammoxidation	Coconut shell	Pre-carbonization: 5 h Carbonization: 2 h Activation: N/A	N/A 500 N/A	1037.0–2995.0	N–H stretching, N–H deformation, and C–N stretching vibrations; pyridinic-N (N-6), pyrrolic-pyridinic-N (N-5), and quaternary-N (N-Q); N–H stretching, N–H deformation, and C–N	100
Urea	Sugarcane bagasse	Pre-carbonization: N/A Carbonization: N/A Activation: 2 h	N/A N/A 800	2905.0	–OH and –COOH; C=C–C C–N, C–O, CN and C=O; O 1s = O–N, O=C and O–C; N 1s = pyridinic-N (N-6), pyrrolic N (N-5), quaternary N (N-Q), and oxidized nitrogen atoms (N-X)	14
Urea	Tamarind shell	Pre-carbonization: 45 min Carbonization: 2 h Activation: N/A	350 800 N/A	410.0	C–C, C=O and C–C=O bonds	12
Urea	Enteromorpha clathrata	Pre-carbonization: 45 min Carbonization: 2 h Activation: N/A	550 800 N/A	97.0–217.3	O–H, C=O, and C=H; C–H and C=N	110
Urea	Chlorella sp. and Spirulina sp.	Pre-carbonization: N/A Carbonization: 2 h Activation: 90 min	95 N/A N/A	5.0–602.8	N–H and/or –OH, CH$_2$, N–H, C=O, and C–N	13
Urea	Orange peel	Pre-carbonization: 24 h Carbonization: 2 h Activation: 90 min	210 N/A 600–700	589.0–590.0	N/A	11

controlled at 550 °C at a heating rate of 5 °C min^{-1} for 60 min and temperature after activation was controlled at 800 °C. Finally, the activation of materials with KOH after pre-carbonization and carbonization of N-doped biomass leads to varying results in functional groups, surface structures, and pore volumes. The presence of N and O atoms in the material plays a crucial role in bonding with C, influencing the material's properties.

5.2. Comparative analysis of chemical activation processes using different methods

5.2.1. Sodium carbonate. Ilnicka and Lukaszewicz synthesized nitrogen-rich nanoporous activated carbon from chitosan using Na_2CO_3 activation.[113] Carbonization (600–900 °C, N_2) and urea doping (for its high N content and solubility) were applied. Activation at 600 °C with 1.93 M Na_2CO_3 resulted in a N_2 content of 2.4–13.1 wt% and surface areas up to 441 m^2 g^{-1} (non-urea), which reduced to 121 m^2 g^{-1} when treated with urea. XPS confirmed C–N bonding (sp^2 and sp^3), including pyridinic (398 eV), pyrrolic (399.8 eV), quaternary (400.9 eV), and oxidized-N species (403.2 eV). The maximum surface area achieved was 1101–1148 m^2 g^{-1} (at 700–800 °C) with 3.5% surface N_2. Ref. 67 prepared activated carbon from poplar wood *via* carbonization at 800–900 °C under N_2 flow. The highest surface area and pore volume reached were ~1580 m^2 g^{-1} and ~0.886 cm^3 g^{-1}, respectively. Functional groups such as C–H, O–H, C–O, C=O, and C=C were found to be present, with –CH–CH$_2$–CH$_3$ indicating aliphatic stretching. Notably, C≡C appeared due to Na_2CO_3 activation, which influenced the functional group composition. Na_2CO_3 activation enhanced material performance and facilitated pyridinic-type N formation, with temperature playing a key role in N-doping.

5.2.2. Activation using orthophosphoric acid. Carbonization with N-doping followed by chemical activation using orthophosphoric acid (H_3PO_4) has been widely studied for biomass processing. H_3PO_4 is often chosen for its ability to enhance the structural properties. Ref. 112 synthesized activated carbon *via* single-step H_3PO_4 activation, followed by urea doping as an N_2 precursor and pyrolysis at 1000 °C. Carbonization was performed under a N_2 flow at 550 °C for 1 hour with a heating rate of 10 °C min^{-1}, yielding a surface area of 1216 m^2 g^{-1} and a pore volume of 1.15 cm^3 g^{-1} (72% yield). XPS analysis confirmed the presence of C 1s (284.3 eV), P 2p (133 eV), O 1s (532 eV), and N 1s (400 eV). Ref. 114 evaluated protein adsorption using H_3PO_4-activated carbon derived from coconut shells. Carbonization under N_2 at 500 °C for 40 minutes produced activated carbon with a surface area of 642 m^2 g^{-1}. H_3PO_4 effectively modified the structure of the precursor and carbon texture. Similarly, Ref. 115 reported surface areas of 1737–1211 m^2 g^{-1} at 400 °C, while cotton stalk-derived carbon exhibited surface areas of 330–1720 m^2 g^{-1} and total pore volumes of 0.15–1.23 cm^3 g^{-1}, with mesopore volumes of 0–0.61 cm^3 g^{-1}. Ref. 64 investigated H_3PO_4 co-carbonization of cellulose with lysine, melamine, chitosan, and dicyandiamide, achieving N contents of 2–12 wt%. XPS analysis identified dominant pyrolytic-N, including pyridinic-N (398.3 eV) and pyrrolic-N

(400.2 eV). The addition of H_3PO_4 influenced lysine formation and increased the conversion rate to 78%. Its strong acidic behavior promoted mesopore formation by degrading the solid matrix, significantly enhancing porosity.

5.2.3. Carbonization followed by zinc chloride. Carbonization with N-doping followed by zinc chloride ($ZnCl_2$) activation has been employed to produce activated carbon from biomass, showing promising potential for energy storage applications.[14,110,116–119] Table 4 provides data on the impact of $ZnCl_2$ activation on capacitance and surface area. Ref. 110 investigated activated carbon derived from *Enteromorpha clathrata* using $ZnCl_2$ activation under an N_2 atmosphere. Samples were heated to 800 °C at a rate of 5 °C min^{-1} and maintained for 60 minutes. The resulting surface area and pore volume for urea- and $ZnCl_2$-treated samples were 217.27 m^2 g^{-1} and 0.327 cm^3 g^{-1}, respectively.

Urea combined with $ZnCl_2$ resulted in a surface area of 188.89 m^2 g^{-1} and a pore volume of 0.30 cm^3 g^{-1}, while urea combined with KOH produced a surface area of 144.81 m^2 g^{-1} with the same pore volume. Notably, all pore diameters remained consistent, ranging from 3.82 to 3.83 nm. $ZnCl_2$ demonstrated superior porous structure formation, aligning with ref. 122 findings that $ZnCl_2$ enhances pore development by acting as a structural scaffold during catalytic dehydration at high temperatures. Additionally, $ZnCl_2$ reacts with hydrogen and oxygen on the material's surface, forming H_2O and H_2.[123] The presence of $ZnCl_2$ also enhances C=N functional groups, while higher temperatures play a crucial role in interlinked pore formation. Zinc ions disrupt the carbon skeleton, promoting internal pore development.[124] Ref. 125 reported that $ZnCl_2$ activated biomass from water hyacinth at 700 °C exhibited high concentrations of pyridinic, pyrrolic, and graphitic nitrogen, confirming excellent electrocatalytic activity. These findings highlight how different activation methods influence the functional groups within the material's framework. Furthermore, ref. 126 utilized bio-oil from biomass thermal conversion to synthesize N-doped hierarchically porous carbon *via* one-step $ZnCl_2$ activation, achieving a surface area of 920.57 m^2 g^{-1} and a large pore volume of 0.55 cm^3 g^{-1}. Mesopore and micropore volumes were measured at 0.385 cm^3 g^{-1} and 0.163 cm^3 g^{-1}, respectively, with high porosity ranging from 86.28% to 91.56%. Functional groups identified included C=O, C=C, O–C=O, and C/C–N.[127] Overall, $ZnCl_2$ effectively enhances surface properties by introducing functional groups and facilitating a well-distributed mesoporous structure. It serves as a valuable activator for N-doped carbonization, with temperature regulation playing a key role in optimizing the pore size distribution.

5.2.4. Activation using potassium carbonate. This section discusses N-doped carbonization followed by chemical activation using potassium carbonate (K_2CO_3).[128–131] Ref. 129 prepared activated carbon from waste medium-density fiberboard, which contains aldehyde resin as an adhesive, for electrode material applications. XPS analysis identified nitrogen species within graphene layers, including N-6 (pyridinic N_2), N-5 (pyrrolic and pyridinic N_2), N-Q (quaternary N_2), and N-X (oxidized N_2). The surface area ranged from 817 to 1027 m^2 g^{-1}, with an average

Table 4 Chemical activation of derived biomass with ZnCl$_2$

Nitrogen doping	Green materials	Synthesis methods	Carbonization (°C)	Surface areas (m^2 g^{-1})	Functional groups	Ref.
NH$_3$	Saw dust	Carbonization: 1 h Activation: N/A	600, 700, and 800 125 (5 °C min^{-1})	281.8–964.9	O–H, C–O, O–H, C=C, and C–N=C	116
Urea	Pomegranate husk	Carbonization: 2 h Activation: 24 h	800 (5 °C min^{-1}) 60	445–1755	Pyridinic-N, pyrrolic-N (N-5), quaternary-N (N-Q)	117
Urea	Jujube shell	Carbonization: 4 h Activation: N/A	900	—	C=O, C–H, C–N	118
Urea	Sugarcane bagasse	Carbonization: 2 h Activation: N/A	800	973–1506	C=C, pyridinic–N, pyrrolic-N, quaternary-N	120
Urea	*Citrus aurantium* waste leaves	Carbonization: 8 h Activation: N/A	120	346–937	C–N, N–H, N–H	121

value of 800 m^2 g^{-1}. The electrodes exhibited capacitances between 147 and 223 F g^{-1} at a current density of 0.5 A g^{-1}. Ref. 130 investigated activated carbon derived from coconut shells, modified with K$_2$CO$_3$ and urea. Activation was conducted at 600 °C for 1 hour under an N$_2$ flow rate of 400 mL min^{-1}, with a heating rate of 5 °C min^{-1}. The surface area of N-doped samples ranged from 947 to 1430 m^2 g^{-1}, while the total pore volume and micropore volume were 0.35–0.65 cm^3 g^{-1} and 0.34–0.58 cm^3 g^{-1}, respectively. Activation at 900 °C significantly increased the micropore volume. The electric double-layer properties of K$_2$CO$_3$-activated carbon were influenced by carbonization and activation parameters, including temperature, duration, and K$_2$CO$_3$ concentration. Nitrogen content ranged from 0.93% to 2.86%, while the specific surface area and capacitance varied between 569 and 1027 m^2 g^{-1} and 147–223 F g^{-1}, respectively. Additionally, ref. 132 studied activated carbon derived from waste tea, investigating the effects of K$_2$CO$_3$ activation at different temperatures and durations. The highest surface area, 1722 m^2 g^{-1}, was achieved at 900 °C, surpassing other studies at lower temperatures. These findings confirm that K$_2$CO$_3$ activation plays a crucial role in enhancing porosity, with temperature optimization being a key factor in achieving high-performance materials.

5.3. Physical activation

Physical activation generally involves two stages: an initial carbonization step at 400–500 °C, followed by activation using steam or CO$_2$ at 900–1000 °C.[133] The activation temperature significantly influences the specific surface area, making physical activation a widely studied, cost-effective method. This process enhances adsorption capacity by developing a porous network in biochar, yielding specific surface areas between 1000 and 1500 m^2 g^{-1} with a pore volume of less than 1 cm^3 g^{-1}.[134] Additionally, physical activation removes residual impurities from the pores formed during carbonization. The CO$_2$ reaction with carbon produces CO, CO$_2$, H$_2$, and CH$_4$, contributing to pore enlargement. However, physical activation has drawbacks, including substantial mass loss, low mechanical strength, and a limited carbon yield.[96] Despite these challenges, it is considered a cleaner alternative to chemical activation and remains a viable low-cost approach with high adsorption capacity and reduced weight loss.

Recent studies have explored N-doping followed by NH$_3$ activation of biomass to produce activated carbon, as summarized in Table 5. For example, ref. 135 synthesized activated carbon from pine sawdust *via* NH$_3$ activation at 700–900 °C for 2 hours. The activated material, mixed with conductive graphite and polyvinylidene fluoride (PVDF) in *N*-methyl-2-pyrrolidone (NMP) at an 8 : 1 : 1 ratio, was treated with NH$_3$ and air at controlled flow rates (NH$_3$: 100 mL min^{-1}; NH$_3$/air: 50 mL min^{-1} with 21% O$_2$). The specific surface area was 757 m^2 g^{-1} and the micropore volume was 0.42 cm^3 g^{-1}. XRD analysis confirmed the presence of graphite-like carbon, while functional groups included C=O, C–C, C–O, O–H, and –NH. Similarly, ref. 136 developed activated carbon from Moso bamboo (*Phyllostachys edulis*) *via* NH$_3$ activation at 200–300 °C, followed

Table 5 Physical activation of synthesized material *via* N-doping methods

N-doping	Physical activation	Precursor	Synthesis methods	Carbonization (°C)	Surface areas (m² g⁻¹)	Functional groups	Ref.
NH₃	Air oxidation	Pine sawdust	Carbonization: 12 h; Activation: N/A	700, 800, and 900	757	C=O, C–O, C–N and C=C; pyridinic-N (N-6), pyrrolic-N (N-5), quaternary-N (N-Q), and oxidized-N (N-X)	135
NH₃	NH₃ (Torrefaction)	Moso bamboo (*Phyllostachys edulis*)	Carbonization: 12 h; Activation: N/A	450, 550, 650, and 750; 200, 250, and 300	N/A	-COO-, -C=O, and C-OH	136
NH₃	NH₃	Crop straw	Carbonization: 3 h; Activation: 2–3 h	600, 700 and 800	72.70 (600 °C) to 418.70 (800 °C)	Pyridinic-N, pyrrolic/pyridonic-N, and oxidized N	138
Urea	CO₂	Coconut leaf	Carbonization: 3 h; Activation: 1 h	700; 800	419	C=C, C–OH, C=O, C=O, C–OH, and C–O–C	40
N/A	CO₂	Bean pulp	Carbonization: 3 h; Activation: 1 h	800	558.20	O–C, C=O, –C–N, N–H, C–O, C=O, C–O–C, pyridinic N, pyridonic N, graphitic N, and oxidized N	139
N/A	CO₂	Water-caltrop shell	Carbonization: 2 h; Activation: 3 h	750; 800–950	N/A	Oxidized N, and graphitic-N	140
NH₃	Steam	Bamboo charcoal	Carbonization: 120 min	600; 850–950	2032	Pyridinic-N, pyrrolic-N atoms, quaternary-N, and N-oxides	141
Urea	Water steam	Peach stones	Carbonization: 30 min	550; 700–750	846	N/A	142

by tube furnace heating at 450–750 °C. The resulting material exhibited N-functional groups (pyridinic-N, pyrrolic-N, and quaternary-N) and oxygen-containing groups (–C=O, C=OH, and –COO–), with N-functional contributions exceeding 85%. NH radicals (NH*) played a key role in functionalization by reacting with bamboo-derived materials.

Sun F., *et al.* heated 3 g of raw coal at 800 °C for 2 hours in an NH_3/N_2 mixture (1 : 1 ratio) at a heating rate of 5 °C min⁻¹.[137] The specific surface area and pore volume were 1235 m² g⁻¹ and 0.58 cm³ g⁻¹, respectively, with functional groups including C–H, O–H, N–H, C–N, and C=O. Ref. 138 Pyrolyzed crop straw at 600 °C for 2 hours, replacing N_2 with NH_3 for N-doping at 600 °C for 1 hour, resulting in surface areas of 72.7–418.7 m² g⁻¹.

Physical activation involves low-temperature carbonization (600 °C) followed by high-temperature activation (800–900 °C). The interaction of high-temperature gases with the material promotes pore formation, while water vapor, CO_2, and other gases contribute to structural stability. These processes highlight the role of physical activation in developing high-performance porous carbon materials.

Prauchner *et al.* activated coconut shells using CO_2,[96] first heating them under N_2 at 850 °C for 2 hours, followed by carbonization at 750 °C with CO_2. This process resulted in narrow pores (<0.7 nm) and 3% CO_2 saturation at 0 °C. Physical activation involves gas diffusion into the carbon material's pores, leading to surface reactions. Temperature and CO_2 flow rate have a significant impact on surface properties, affecting both electrical conductivity and pore structure. While chemical activation produces larger surface areas, both physical and chemical activation influence the pore distribution and electronic properties, enhancing performance in energy storage applications like Li-ion batteries and fuel cells.

According to the review above regarding the chemical and physical activation, we have concluded the key points below: ammoxidation with alkaline activation (KOH) is highly efficient in creating high specific surface areas (up to 2995 m² g⁻¹) and well-developed porous structures, which are crucial for supercapacitor applications. The method also introduces functional groups like C=O, C–O–C, and C–O–H, which enhance the electrochemical capacitance through faradaic reactions. While KOH activation requires high temperatures (700–900 °C), which can lead to a decrease in micropore percentage at higher temperatures. This trade-off between the surface area and pore size distribution needs to be carefully managed depending on the application. Activation using sodium carbonate (Na_2CO_3) is less aggressive compared to KOH, resulting in lower surface areas (up to 1148 m² g⁻¹) but with a higher nitrogen content (up to 13.1 wt%). The lower surface area compared to KOH activation may limit its use in applications requiring high surface area. However, the higher nitrogen content can be advantageous for specific electrochemical applications where redox activity is more critical than the surface area. Activation using orthophosphoric acid (H_3PO_4) is effective in creating mesoporous structures with surface areas ranging from 330 to 1720 m² g⁻¹. It also introduces phosphorus and nitrogen functional groups, which can enhance the electrochemical performance. H_3PO_4 activation is particularly useful for creating mesopores,

which are beneficial for electrolyte penetration and ion transport. However, the surface areas are generally lower than those achieved with KOH activation, making it less suitable for applications requiring very high surface areas. Activation using zinc chloride ($ZnCl_2$) is effective in creating a well-developed pore structure with surface areas up to 1755 m^2 g^{-1}. It also introduces nitrogen functional groups, which are beneficial for electrochemical applications. $ZnCl_2$ activation is comparable to KOH in terms of surface area and pore structure development. However, it may require careful control of temperature to avoid excessive pore widening, which can reduce the material's effectiveness in certain applications. Activation using potassium carbonate (K_2CO_3) can produce surface areas up to 1430 m^2 g^{-1} and introduces nitrogen functional groups. It is effective in creating microporous structures, which are beneficial for high capacitance. K_2CO_3 activation is less aggressive than KOH, resulting in lower surface areas but with better control over pore size distribution. This makes it suitable for applications where a balance between surface area and pore size is critical.

Physical activation (CO_2 and steam): physical activation methods, such as CO_2 and steam activation, can produce surface areas up to 2032 m^2 g^{-1}. Physical activation is less efficient in creating high surface areas and have less control over the pore structure compared to chemical activation methods. However, it is more environmentally friendly and cost-effective, making it suitable for large-scale applications where high surface area is not the primary requirement. CO_2 activation is effective in creating narrow pores (less than 0.7 nm) and can produce surface areas up to 850 m^2 g^{-1}. Although CO_2 activation is less efficient in creating high surface areas compared to chemical activation methods, it is particularly useful for applications requiring narrow pores and is more environmentally friendly.

As concluded above, KOH and $ZnCl_2$ activation are the most efficient in creating high surface areas, making them suitable for supercapacitor applications where high surface area is critical. While H_3PO_4 and $ZnCl_2$ activation are effective in creating mesoporous structures, which are beneficial for electrolyte penetration and ion transport. Physical activation methods (CO_2 and steam) are more environmentally friendly and cost-effective but generally result in lower surface areas and less control over the pore structure. The choice of activation method

depends on the specific requirements of the application. Future studies should focus on optimizing these methods to balance the surface area, pore structure, and functional group introduction for specific applications.

5.4. AI-assisted preparation of nitrogen-doped biochar

Recent advancements in artificial intelligence (AI) have significantly contributed to the optimization of nitrogen-doped (N-doped) biochar materials for energy storage applications. Machine learning (ML) techniques, such as Random Forest (RF)[143] and Extreme Gradient Boosting (XGBoost),[144] have been employed to predict the specific capacitance of N-doped biochar. These models utilize a comprehensive set of features, including pore structure parameters, elemental composition, N-containing functional groups, and electrochemical testing characteristics. To better understand how these features influence capacitance, Shapley additive explanations and partial dependency plots were applied. The results demonstrated exceptional predictive performance, with R^2 values of 0.95 for RF and 0.96 for XGBoost. Notably, among the three N-containing groups, N-6 was identified as the most significant contributor to higher specific capacitance. Partial dependency plot analysis further revealed that optimal conditions for enhanced capacitive performance occur when the specific surface area is approximately 2200 m^2 g^{-1}, the pore size is around 4 nm, and the degree of graphitization is about one. Beyond traditional ML approaches, deep learning models have also been explored for biochar characterization. A Convolutional Neural Network (CNN) based on the DenseNet architecture was developed to enhance the predictive accuracy. The CNN model consisted of an input layer and two hidden layers employing the ReLU (Rectified Linear Unit) activation function to introduce non-linearity, enabling the model to learn complex patterns efficiently. This approach allows for advanced feature extraction, leveraging DenseNet's strength in improving the model performance (Fig. 5).

6. Density functional theory (DFT) of N-doping materials

DFT plays a crucial role in elucidating the relationship between N-doping and carbon materials by enabling the calculation of
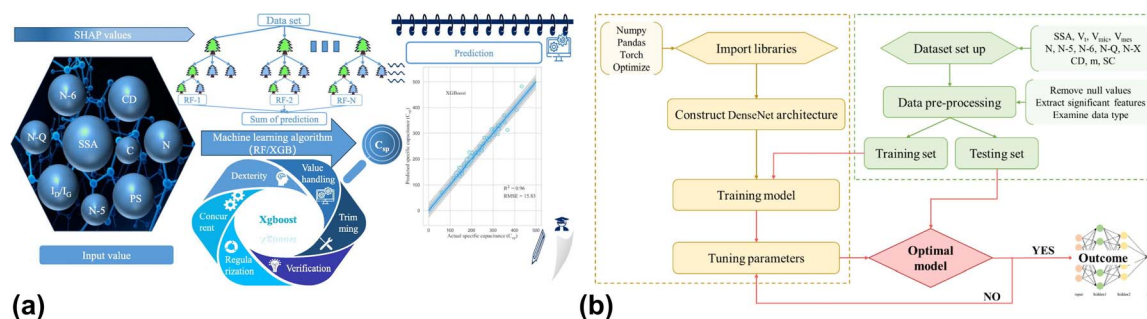

Fig. 5 (a) Machine learning prediction of supercapacitor performance of N-doped biochar from biomass wastes based on N-containing groups, elemental compositions, and pore structures. (b) Workflow of the convolutional neural network modeling process of nitrogen-doped porous biochar.

structural and interfacial characteristics governing adsorbent–molecule interactions[76,145,146] and usually focused on the formation energy and chemical potential (μ) associated with pyridinic-N and pyrrolic-N.[147] Mostly, the surface contains–OH and –COOH and appears as –COOH, –OH, and –NH_2,[148] sometimes overlapping with O–H at N–H present in materials.[148] This is associated with electrostatic and hydrogen-bonding interactions, with π–π, electrostatic, and H2 interactions. DFT calculation results confirmed that pyridinic-N species for N-doping carbon materials is associated with the CO_2RR.[149] Interactions of the chemical or targets with MNB include π–π, electrostatic, and hydrogen bonding interactions. Generally, the formation energy of pyridinic-N is lower than graphene under N-rich conditions, which indicated that the hybrid is more beneficial for obtaining active pyridinic-N sites. Electrons of pyridinic-N play a major role in releasing the *COOH intermediate, where it enhances the CO_2RR catalytic activity, containing active origin pyridinic-N sites.[150] Also, pyrrolic nitrogen plays a pivotal role in improving the capacitance of materials, especially for the supercapacitors. In terms of graphitic-N, it improves the quantum capacitance. Conversely, pyrolytic improvement is associated with total capacitance because of its lower quantum capacitance.[151] From this point of view, controlling the type and concentration of N-doping is suggested during carbonization and activation to optimize the capacitance because higher total quantum capacitance has a direct impact on the total capacitance, as suggested by ref. 151. In further analysis, calculation of DFT will give important information related to the structure of the material itself precisely, where one can refer to for appropriate control of types and concentrations of N-doping.[152]

Table 6 identifies the fitted peaks of parameters from the XPS spectrum associated with the functional groups from N-doping activation. The N 1s spectrum with different peaks represents the existence of pyridinic N, pyrrolic N, pyridinic-N-oxide, graphitic N, and quaternary N, as a result of N-doping carbonization. Mostly, N-rich carbon materials, which are synthesized via nitridization of carbon precursors or direct N-containing materials, contribute to N and multi-species, such as N-5, N-6t, N-Q and N-X. The N species present provides electron donors on the carbon layers, confirming the role of electrochemical carbon and active sites in the pseudocapacitive reactions, for the electrochemical storage applications. Moreover, the presence of N-species indicates a greater electrochemical performance. As a result, the combination of capacitance and pseudocapacitance has an impact on the largest specific capacitances of the material itself.[153] Ref. 154 also demonstrated that pyridinic nitrogen improves the capacitance related to material design and synthesis. Furthermore, N-doping provides more active sites, more O_2 vacancies, high surface areas, and improved morphology. It provides the effect of N_2 on the electronic properties, catalytic activity, reaction mechanism and stabilization of N-doped carbon. In this case, characterization of materials via XPS identified peaks of the parameters associated with the assignment. Different types of biomass are formed with different porous structures, depending on the treatment of biomass itself as a result of N-doping treatment. Thus, it is clear that N-doping presents materials with different characteristics for energy storage applications.

DFT calculations demonstrate that nitrogen doping, particularly pyridinic-N and pyrrolic-N in carbon materials, significantly enhances the adsorption ability of potassium ions, leading to improved potassium storage performance.[155] Three N-doping models—N-5, N-6, and NQ—were analyzed by placing potassium atoms at different positions in each model to calculate adsorption energies. The results showed that the ΔE_a values of N-5 (-2.63 eV) and N-6 (-2.86 eV) were higher than that of NQ (0.14 eV), indicating that pyrrolic- and pyridinic-N-doping enhance the potassium adsorption capacity more than graphitic-N-doping.[156] Among the models, N-6 doping exhibited the lowest ΔE_a, with the highest electron density and consequently a greater K^+ adsorption capacity. This capacity was further enhanced with an increase in N-doping content. Additionally, N-doping improves the electrochemical properties and performance of hard carbon materials. Nitrogen-doping

Table 6 Fitted XPS N 1s peak parameters and corresponding nitrogen species assignments in N-doped materials

Elements	Precursor	E_g (eV)	Assignments	Ref.
N 1s	Soybean	398.5	Pyridinic-N	15
N 1s	Soybean	401.2	Graphitic-N	15
N 1s	Corncob	398.1	Pyridinic-N	109
N 1s	Corncob	399.4	Ph–NH_2	109
N 1s	Sugarcane bagasse	398.2	Pyridinic-N (N-6)	14
N 1s	Sugarcane bagasse	399.7	Pyrrolic-N (N-5)	14
N 1s	Sugarcane bagasse	401.2	Quaternary-N (N-Q)	14
N 1s	Sugarcane bagasse	403.0	Oxidized nitrogen atoms (N-X)	14
N 1s	Tamarind shell	401.5	Pyridinic-N	12
N 1s	Tamarind shell	404.2	Pyrrole-like nitrogen	12
N 1s	Licorice root	398.4	Pyridinic-N (N-6)	17
N1 s	Licorice root	400.7	Pyrrolic-N (N-5)	17
N 1s	Licorice root	401.5	Quaternary-N (N-Q)	17
N 1s	Licorice root	402.9	Pyridinic-N-oxide (N-6)	17
N 1s	Water hyacinth	401.2	Graphitic-N	125
N 1s	Water hyacinth	399.2	Pyrrolic-N	125
N 1s	Water hyacinth	398.4	Pyridinic-N	125

configurations like pyridinic-N, pyrrolic-N, and graphitic-N have distinct effects on K-ion absorption and migration, which ultimately affect the overall performance of the materials. DFT simulations of N-doped graphene show enhanced properties for supercapacitors when graphene is doped with graphitic, pyrrolic, or pyridinic nitrogen.[157] N-doping also helps reduce volume expansion during the simulation process, which is typically responsible for poor cell performance, as indicated by DFT results. In the context of CO_2 capture, DFT calculations also reveal that nitrogen-doped carbon materials exhibit significantly higher CO_2 adsorption compared to pristine carbon. Nitrogen doping alters the local charge distribution and density of states (DOS), improving the CO_2 adsorption performance. Specifically, the CO_2 adsorption energies for N-6 (G P-N 6), N-5 (G P-N 5), and NQ (G P-N Q) were calculated as −2.57 eV, −1.79 eV, and −0.28 eV, respectively. This shows that G P-N 6 and G P-N 5 have a stronger tendency to adsorb CO_2. N-doping increases the dispersion and electrostatic interactions between CO_2 and biochar, with higher nitrogen content leading to more pronounced improvement in the adsorption performance.[158]

7. Challenges, perspectives, and future prospects of N-doped green materials

The development of nitrogen-doped (N-doped) green materials holds immense promise, yet several technical challenges persist. One major challenge lies in optimizing the nitrogen content while preserving the structural integrity of the carbon framework. A delicate balance must be achieved as excess nitrogen can weaken the carbon network, while insufficient doping reduces the number of electrochemically active sites, ultimately impacting the specific capacitance and performance. Additionally, thermal instability during high-temperature chemical activation, such as KOH treatment, often results in nitrogen volatilization, diminishing the overall nitrogen content and associated functionalities. Another critical challenge is controlling porosity and pore size distribution. The electrochemical performance and CO_2 adsorption capacity of these materials strongly depend on a well-developed and hierarchical pore structure. However, precisely tailoring the balance between micropores, which enhance adsorption, and mesopores, which facilitate ion transport, remains difficult. Furthermore, transitioning from lab-scale synthesis to industrial production is hindered by scalability and cost-efficiency concerns. High energy inputs and expensive activating agents pose obstacles to the economic viability of these materials. In capacitive deionization (CDI) applications, a trade-off exists between ion storage and mobility—micropores improve ion adsorption but limit transport, whereas mesopores offer enhanced diffusion but may compromise the capacity. Achieving an optimal pore architecture for CDI performance is therefore essential.

Despite these challenges, promising perspectives emerge for advancing N-doped biomass-derived materials. Biomass offers an abundant, low-cost, and sustainable precursor for producing functional carbon materials suitable for energy storage, CO_2 capture, and CDI. The introduction of nitrogen-rich compounds such as urea during synthesis has shown to enhance nitrogen retention and improve the resulting material's electrochemical behavior. Modifying activation conditions—such as temperature and time—also allows for tuning the pore structure and maximizing the specific capacitance. Nitrogen configurations like pyridinic-N, pyrrolic-N, and graphitic-N have been identified as key contributors to enhance the conductivity, charge storage, and redox activity, while oxygen-containing groups (e.g., C=O and C–O) further contribute to capacitive behavior. Controlling the activation temperature is especially crucial. For instance, thermal treatment in the range of 700–900 °C is often optimal for achieving high surface areas, mesoporous structures, and desirable C/O ratios. Chemical activation, particularly with KOH, can yield specific surface areas exceeding 2900 m^2 g^{-1}, significantly enhancing the electrochemical and adsorption performance.

Looking ahead, several future prospects are expected to shape the evolution of N-doped green materials. Research into advanced modification strategies, including dual or tri-doping with heteroatoms, such as sulfur, phosphorus, or boron, could lead to synergistic effects that boost material performance. Furthermore, developing scalable, energy-efficient, and low-cost synthesis routes is essential for commercial deployment in applications like supercapacitors, lithium-ion batteries, and CO_2 capture systems. The integration of N-doped materials with emerging technologies including hybrid capacitors, metal–air batteries, and next-generation energy storage platforms offers exciting opportunities for multifunctional and high-efficiency devices. Additionally, expanding the range of biomass precursors beyond traditional sources to include algae, agricultural waste, and industrial by-products may further enable the tailoring of pore structure, conductivity, and surface chemistry for specific application demands. These advancements will be instrumental in bridging the gap between lab innovation and real-world impact, aligning green material development with global sustainability goals.

8. Conclusion

In this review, the synthesis of N-doping from especially plants has been explored to understand its process and results, involving pre-carbonization, carbonization followed by activation through chemical and physical methods to adjust its surface area, functional groups and specific kind of N-doping. Various carbonization and activation methods, including chemical and physical activation, have a direct impact on surface materials. The presence of pyridinic N, graphitic N, and oxidized N in the material confirms the role of N_2 in material carbonization. After carbonization using different activation methods, functional groups such as C=O, C–C, C–O, C–N, C–H, C–O–C, C–H, –OH, graphitic N, pyrrolic N, pyridinic N, and quaternary N are observed in the material. However, the resulting surface area and capacitances vary significantly for energy storage applications. Porous N-doping derived from biomass enhances activated porous carbon by increasing the

surface area and enhancing electrochemical catalytic reactions, providing more active sites and electronic conductivity for energy storage applications. The electrocatalytic activity, particularly the oxygen reduction reaction (ORR), is associated with the presence of N functional groups in the materials.

Chemical activation using KOH is widely used to create surface area. Additionally, DFT calculations are recommended to determine the structure and characteristics of molecules in the materials, confirming electrostatic and hydrogen bonding interactions. Future research on N-doping porous carbons should focus on DFT analysis, especially post-carbonisation and post-activation methods, to obtain crucial information for material design. Recycling methods for the material itself should be studied to assess the quality. Plasma treatments further investigate surface areas of biomass-derived materials post-treatment, considering additional chemical and physical activation methods for further utilization. Additionally, expanding material applications beyond energy storage to include CO_2 adsorption, CDI, and battery applications is recommended.

Author contributions

Conflicts of interest

There are no conflicts to declare.

Data availability

No primary research results, software or code have been included and no new data were generated or analysed as part of this review.

Acknowledgements

References

1 N. K. Arora and I. Mishra, *Environ. Sustainability*, 2022, **5**, 395–399.

2 T. Khandaker, T. Islam, A. Nandi, M. A. A. M. Anik, M. S. Hossain, M. K. Hasan and M. S. Hossain, *Sustainable Energy Fuels*, 2025, **9**, 693–723.

3 J. Mu, S. I. Wong, Q. Li, P. Zhou, J. Zhou, Y. Zhao, J. Sunarso and S. Zhuo, *J. Alloys Compd.*, 2020, **832**, 154950.

4 L. Qin, Z. Zhou, J. Dai, P. Ma, H. Zhao, J. He, A. Xie, C. Li and Y. Yan, *J. Taiwan Inst. Chem. Eng.*, 2016, **62**, 228–238.

5 A. K. Mondal, K. Kretschmer, Y. Zhao, H. Liu, H. Fan and G. Wang, *Microporous Mesoporous Mater.*, 2017, **246**, 72–80.

6 Y. Deng, J. Chen, Z. Xiao, J. Liu, J. Zhang, B. Zhu, X. You, F. Ni, T. Ao and Y. Tan, *Water, Air, Soil Pollut.*, 2024, **235**, 133.

7 L. Feng, X. Li, X. Chen, Y. Huang, K. Peng, Y. Huang, Y. Yan and Y. Chen, *Sci. Total Environ.*, 2020, **708**, 135071.

8 T. Liamprawat, P. Verasarut, N. Kaewtrakulchai, G. Panomsuwan, M. Fuji and A. Eiad-Ua, *Mater. Sci. Forum*, 2020, **990**, 155–160.

9 B. Yang, J. Gao, M. Xie, S. Zuo, H. Kang, Y. Sun, X. Xu, W. Wang, C. Gao, Y. Liu and J. Yan, *J. Colloid Interface Sci.*, 2020, **579**, 832–841.

10 M. Gao, C.-C. Shih, S.-Y. Pan, C.-C. Chueh and W.-C. Chen, *J. Mater. Chem. A*, 2018, **6**, 20546–20563.

11 K. Xiao, H. Liu, Y. Li, G. Yang, Y. Wang and H. Yao, *Chem. Eng. J.*, 2020, **382**, 122997.

12 V. Muthukumaraswamy Rangaraj, A. Achazhiyath Edathil, Y. Y. Kannangara, J.-K. Song, M. Abu Haija and F. Banat, *J. Electroanal. Chem.*, 2019, **848**, 113307.

13 S. Shi and Y. Liu, *Fuel*, 2021, **306**, 121762.

14 K. Zou, Y. Deng, J. Chen, Y. Qian, Y. Yang, Y. Li and G. Chen, *J. Power Sources*, 2018, **378**, 579–588.

15 G. Lin, R. Ma, Y. Zhou, Q. Liu, X. Dong and J. Wang, *Electrochim. Acta*, 2018, **261**, 49–57.

16 A. J. C. Mary, C. Nandhini and A. C. Bose, *Mater. Lett.*, 2019, **256**, 126617.

17 J. Gao, D. Fan and X. Liu, *New J. Chem.*, 2021, **45**, 15469–15474.

18 Z. Bi, Q. Kong, Y. Cao, G. Sun, F. Su, X. Wei, X. Li, A. Ahmad, L. Xie and C.-M. Chen, *J. Mater. Chem. A*, 2019, 7, 16028–16045.

19 G. Tang, W. Qiao, Z. Wang, F. Liu, L. He, M. Liu, W. Huang, H. Wu and C. Liu, *Green Chem.*, 2023, **10**, 3738–3766.

20 S. Chawla, P. Rai, T. Garain, S. Uday and C. M. Hussain, *Trends Environ. Anal. Chem.*, 2022, **33**, e00156.

21 C. P. T. Devatha and K. Arun, in *Synthesis of Inorganic Nanomaterials*, 2018, pp. 169–184, DOI: **10.1016/b978-0-08-101975-7.00007-5**.

22 S. Kumar, G. Saeed, L. Zhu, K. N. Hui, N. H. Kim and J. H. Lee, *Chem. Eng. J.*, 2021, **403**, 126352.

23 N. Yan and X. Chen, *Nature*, 2015, **524**, 155–157.

24 P. Liu, Y. Wang and J. Liu, *J. Energy Chem.*, 2019, **34**, 171–185.

25 S. S. Sekhon, P. Kaur and J.-S. Park, *Renewable Sustainable Energy Rev.*, 2021, **147**, 111173.

26 P. Feng, J. Li, H. Wang and Z. Xu, *ACS Omega*, 2020, **5**, 24064–24072.

27 Y. Deng, Y. Xie, K. Zou and X. Ji, *J. Mater. Chem. A*, 2016, **4**, 1144–1173.

28 L. Dai, Y. Xue, L. Qu, H. J. Choi and J. B. Baek, *Chem. Rev.*, 2015, **115**, 4823–4892.

29 M. Gao, C. C. Su, M. He, T. Glossmann, A. Hintennach, Z. Feng, Y. Huang and Z. Zhang, *J. Mater. Chem. A*, 2017, **14**, 6725–6733.

30 F. Rodriguez-Reinoso and M. Molina-Sabio, *Carbon*, 1992, **30**, 1111–1118.

31 N. Mohamad Nor, L. C. Lau, K. T. Lee and A. R. Mohamed, *J. Environ. Chem. Eng.*, 2013, **1**, 658–666.

32 P. González-García, *Renewable Sustainable Energy Rev.*, 2018, **82**, 1393–1414.

33 R. C. Sanito, C. Lidwina, H. H. Yang and Y. F. Wang, *Heliyon*, 2022, **8**, e11240.

34 M. Danish and T. Ahmad, *Renewable Sustainable Energy Rev.*, 2018, **87**, 1–21.

35 M. A. Yahya, Z. Al-Qodah and C. W. Z. Ngah, *Renewable Sustainable Energy Rev.*, 2015, **46**, 218–235.

36 K. Ukanwa, K. Patchigolla, R. Sakrabani, E. Anthony and S. Mandavgane, *Sustainability*, 2019, **11**, 6204.

37 O. Ioannidou and A. Zabaniotou, *Renewable Sustainable Energy Rev.*, 2007, **11**, 1966–2005.

38 M. A. Yahya, M. H. Mansor, W. A. A. W. Zolkarnaini, N. S. Rusli, A. Aminuddin, K. Mohamad, F. A. M. Sabhan, A. A. A. Atik and L. N. Ozair, *AIP Conf. Proc.*, 2018, 030023.

39 S. V. Vassilev, D. Baxter, L. K. Andersen and C. G. Vassileva, *Fuel*, 2010, **89**, 913–933.

40 S. Wang, Z. Ren, J. Li, Y. Ren, L. Zhao and J. Yu, *RSC Adv.*, 2014, **4**, 31300–31307.

41 J. J. Lado, R. L. Zornitta, I. Vázquez Rodríguez, K. Malverdi Barcelos and L. A. M. Ruotolo, *ACS Sustain. Chem. Eng.*, 2019, **7**, 18992–19004.

42 L. Sun, Y. Gong, D. Li and C. Pan, *Green Chem.*, 2022, **24**, 3864–3894.

43 C. Ruan, K. Ai and L. Lu, *RSC Adv.*, 2014, **4**, 30887–30895.

44 G. Ma, Q. Yang, K. Sun, H. Peng, F. Ran, X. Zhao and Z. Lei, *Bioresour. Technol.*, 2015, **197**, 137–142.

45 C. O. Ania, V. Khomenko, E. Raymundo-Piñero, J. B. Parra and F. Béguin, *Adv. Funct. Mater.*, 2007, **17**, 1828–1836.

46 D. Hulicova, M. Kodama and H. Hatori, *Chem. Mater.*, 2006, **18**, 2318–2326.

47 B. T. Liu, X. M. Shi, X. Y. Lang, L. Gu, Z. Wen, M. Zhao and Q. Jiang, *Nat. Commun.*, 2018, **9**, 1375.

48 T. Brousse, D. Bélanger and J. W. Long, *J. Electrochem. Soc.*, 2015, **162**, A5185–A5189.

49 M. Zgrzebnicki, V. Nair, S. Mitra, A. Kałamaga, J. Przepiórski and R. J. Wrobel, *Chem. Eng. J.*, 2022, **427**, 131709.

50 C. L. Mangun, K. R. Benak, J. Economy and K. L. Foster, *Carbon*, 2001, **39**, 1809–1820.

51 Z. Wan, Y. Sun, D. C. W. Tsang, E. Khan, A. C. K. Yip, Y. H. Ng, J. Rinklebe and Y. S. Ok, *Chem. Eng. J.*, 2020, **401**, 126136.

52 M. Nandi, K. Okada, A. Dutta, A. Bhaumik, J. Maruyama, D. Derks and H. Uyama, *Chem. Commun.*, 2012, **48**, 10283–10285.

53 M. Li, C. Liu, H. Cao, H. Zhao, Y. Zhang and Z. Fan, *J. Mater. Chem. A*, 2014, **2**, 14844–14851.

54 Y. Gao, W. Gao, H. Zhu, H. Chen, S. Yan, M. Zhao, H. Sun, J. Zhang and S. Zhang, *Int. J. Environ. Res. Public Health*, 2022, **19**, 14805.

55 A. Ilnicka, M. Skorupska, M. Szkoda, Z. Zarach and J. P. Lukaszewicz, *Mater. Res. Lett.*, 2022, **11**, 213–221.

56 J. Hu, Z. Li, A. Zhang, S. Mao, I. R. Jenkinson and W. Tao, *Environ. Res.*, 2020, **188**, 109764.

57 W. Mao, J. Wang, Z. Xu, Z. Niu and J. Zhang, *Electrochem. Commun.*, 2006, **8**, 1326–1330.

58 J. He, D. Zhang, Y. Wang, J. Zhang, B. Yang, H. Shi, K. Wang and Y. Wang, *Appl. Surf. Sci.*, 2020, **515**, 146020.

59 Y. Zhou, S. Liu, Y. Liu, X. Tan, N. Liu and J. Wen, *Int. J. Environ. Res. Public Health*, 2020, **17**, 8377.

60 C. Yan, L. Zhu, J. Dong, D. Gu, H. Jiang and B. Wang, *R. Soc. Open Sci.*, 2019, **6**, 180919.

61 K. Ö. Köse, B. Pişkin and M. K. Aydınol, *Int. J. Hydrogen Energy*, 2018, **43**, 18607–18616.

62 P. E. Hock and M. A. A. Zaini, *Acta Chim. Slovaca*, 2018, **11**, 99–106.

63 F. Cesano, S. Cravanzola, V. Brunella and D. Scarano, *Microporous Mesoporous Mater.*, 2019, **288**, 109605.

64 K. Mainali and M. Garcia-Perez, *J. Anal. Appl. Pyrolysis*, 2023, **169**, 105837.

65 P. Zhao, Y. Shen, S. Ge, Z. Chen and K. Yoshikawa, *Appl. Energy*, 2014, **131**, 345–367.

66 S. M. Yakout and G. Sharaf El-Deen, *Arabian J. Chem.*, 2016, **9**, S1155–S1162.

67 H. Demiral and I. Uzun, *Surf. Interface Anal.*, 2010, **42**, 1338–1341.

68 F. H. Emamy, A. Bumajdad and J. P. Lukaszewicz, *Nanomaterials*, 2021, **11**, 1907.

69 T. E. Brown, H. E. LeMay, B. E. Bursten, C. Murphy, P. Woodward and M. E. Stoltzfus, *Chemistry: the Central Science in SI Units, Global Edition*, Pearson Education, 2021.

70 H. Wang, Y. Shao, S. Mei, Y. Lu, M. Zhang, J.-k. Sun, K. Matyjaszewski, M. Antonietti and J. Yuan, *Chem. Rev.*, 2020, **120**, 9363–9419.

71 Y. Ren, C. Yu, X. Tan, Q. Wei, Z. Wang, L. Ni, L. Wang and J. Qiu, *Energy Environ. Sci.*, 2022, **15**, 2776–2805.

72 J. Lefebvre, J. Ding, Z. Li, P. Finnie, G. Lopinski and P. R. Malenfant, *Acc. Chem. Res.*, 2017, **50**, 2479–2486.

73 C. Wang, H. Dong, L. Jiang and W. Hu, *Chem. Soc. Rev.*, 2018, **47**, 422–500.

74 C.-X. Zhou, J.-X. Sun, Z.-J. Deng and S. Zhou, *Semiconductors*, 2013, **47**, 1351–1357.

75 M. A. Zazycki, P. A. Borba, R. N. F. Silva, E. C. Peres, D. Perondi, G. C. Collazzo and G. L. Dotto, *Adv. Powder Technol.*, 2019, **30**, 1494–1503.

76 D. Adekoya, S. Qian, X. Gu, W. Wen, D. Li, J. Ma and S. Zhang, *Nano-Micro Lett.*, 2020, **13**, 13.

77 H. Miao, S. Li, Z. Wang, S. Sun, M. Kuang, Z. Liu and J. Yuan, *Int. J. Hydrogen Energy*, 2017, **42**, 28298–28308.

78 S. N. Faisal, E. Haque, N. Noorbehesht, W. Zhang, A. T. Harris, T. L. Church and A. I. Minett, *RSC Adv.*, 2017, **7**, 17950–17958.

79 C. Falco, J. P. Marco-Lozar, D. Salinas-Torres, E. Morallon, D. Cazorla-Amorós, M.-M. Titirici and D. Lozano-Castello, *Carbon*, 2013, **62**, 346–355.

80 B. Sajjadi, W.-Y. Chen and N. O. Egiebor, *Rev. Chem. Eng.*, 2019, **35**, 735–776.

81 B. Viswanathan, P. I. Neel and T. K. Varadarajan, *Methods of activation and specific applications of carbon materials*, 2009, vol. 600, pp. 1–160.

82 M. Kodama, J. Yamashita, Y. Soneda, H. Hatori, S. Nishimura and K. Kamegawa, *Mater. Sci. Eng., B*, 2004, **108**, 156–161.

83 J. S. Noh and J. A. Schwarz, *Carbon*, 1990, **28**, 675–682.

84 K. Kaneko, T. Katori, K. Shimizu, N. Shindo and T. Maeda, *J. Chem. Soc., Faraday Trans.*, 1992, **88**, 1305–1309.

85 B. A. Bashkova S and T. J. Bandosz, *Langmuir*, 2003, **19**, 6115–6121.

86 A. Bagreev, J. Angel Menendez, I. Dukhno, Y. Tarasenko and T. J. Bandosz, *Carbon*, 2004, **42**, 469–476.

87 F. Adib, A. Bagreev and T. J. Bandosz, *Langmuir*, 2000, **16**, 1980–1986.

88 W. Chen, F. S. Cannon and J. R. Rangel-Mendez, *Carbon*, 2005, **43**, 573–580.

89 M. Abe, K. Kawashima, K. Kozawa, H. Sakai and K. Kaneko, *Langmuir*, 2006, 5059–5063.

90 M. Seredych, D. Hulicova-Jurcakova, G. Q. Lu and T. J. Bandosz, *Carbon*, 2008, **46**, 1475–1488.

91 J. Lahaye, G. Nanse, A. Bagreev and V. Strelko, *Carbon*, 1999, **37**, 585–590.

92 V. V. Strelko, V. S. Kuts and P. A. Thrower, *Carbon*, 2000, **38**, 1499–1524.

93 B. Stohr, H. P. Boehm and R. Schlogl, *Carbon*, 1991, **29**, 707–720.

94 L. Yan, J. Yu, J. Houston, N. Flores and H. Luo, *Green Energy Environ.*, 2017, **2**, 84–99.

95 Z. Chen, S. Yun, L. Wu, J. Zhang, X. Shi, W. Wei, Y. Liu, R. Zheng, N. Han and B.-J. Ni, *Nano-Micro Lett.*, 2023, **15**, 4.

96 M. J. Prauchner and F. Rodríguez-Reinoso, *Microporous Mesoporous Mater.*, 2012, **152**, 163–171.

97 A. R. Mohamed, M. Mohammadi and G. N. Darzi, *Renewable Sustainable Energy Rev.*, 2010, **14**, 1591–1599.

98 X. Yang, T. Lv and J. Qiu, *Small*, 2023, **19**, e2300336.

99 J. Zhou, P. Yang, P. A. Kots, M. Cohen, Y. Chen, C. M. Quinn, M. D. de Mello, J. Anibal Boscoboinik, W. J. Shaw and S. Caratzoulas, *Nat. Commun.*, 2023, **14**, 2293.

100 L. Guo, J. Yang, G. Hu, X. Hu, L. Wang, Y. Dong, H. DaCosta and M. Fan, *ACS Sustain. Chem. Eng.*, 2016, **4**, 2806–2813.

101 J. Wang and S. Kaskel, *J. Mater. Chem.*, 2012, **22**, 23710.

102 J. M. Dias, M. C. Alvim-Ferraz, M. F. Almeida, J. Rivera-Utrilla and M. Sanchez-Polo, *J. Environ. Manage.*, 2007, **85**, 833–846.

103 E. Raymundo-Piñero, K. Kierzek, J. Machnikowski and F. Béguin, *Carbon*, 2006, **44**, 2498–2507.

104 J. Huang, B. G. Sumpter and V. Meunier, *Chemistry*, 2008, **14**, 6614–6626.

105 L.-Z. Fan, S. Qiao, W. Song, M. Wu, X. He and X. Qu, *Electrochim. Acta*, 2013, **105**, 299–304.

106 L. Zhao, L. Z. Fan, M. Q. Zhou, H. Guan, S. Qiao, M. Antonietti and M. M. Titirici, *Adv. Mater.*, 2010, **22**, 5202–5206.

107 B. E. Conway, V. Birss and J. Wojtowicz, *J. Power Sources*, 1997, **66**, 1–14.

108 D. Hulicova, J. Yamashita, Y. Soneda, H. Hatori and M. Kodama, *Chem. Mater.*, 2005, **17**, 1241–1247.

109 Z. Geng, Q. Xiao, H. Lv, B. Li, H. Wu, Y. Lu and C. Zhang, *Sci. Rep.*, 2016, **6**, 30049.

110 K. Xie, Y. Hu, S. Afonaa-Mensah, C. Yuan, B. Cao, S. Wang and Q. Wang, *J. Renewable Mater.*, 2022, **10**, 541–560.

111 D. W. Wang, F. Li, L. C. Yin, X. Lu, Z. G. Chen, I. R. Gentle, G. Q. Lu and H. M. Cheng, *Chemistry*, 2012, **18**, 5345–5351.

112 M. Borghei, N. Laocharoen, E. Kibena-Põldsepp, L.-S. Johansson, J. Campbell, E. Kauppinen, K. Tammeveski and O. J. Rojas, *Appl. Catal., B*, 2017, **204**, 394–402.

113 A. Ilnicka and J. P. Lukaszewicz, *Mater. Sci. Eng., B*, 2015, **201**, 66–71.

114 R. G. Pereira, C. M. Veloso, N. M. da Silva, L. F. de Sousa, R. C. F. Bonomo, A. O. de Souza, M. O. d. G. Souza and R. d. C. I. Fontan, *Fuel Process. Technol.*, 2014, **126**, 476–486.

115 A. C. Lua and T. Yang, *J. Colloid Interface Sci.*, 2005, **290**, 505–513.

116 M. A. El-Nemr, M. A. Hassaan and I. Ashour, *Biomass Conversion and Biorefinery*, 2022.

117 K. Sun, J. Li, H. Peng, E. Feng, G. Ma and Z. Lei, *Ionics*, 2016, **23**, 985–996.

118 Y. Li and B. Qi, *Electrochem. Commun.*, 2023, **152**, 107512.

119 P. Williams and A. Reed, *Biomass Bioenergy*, 2006, **30**, 144–152.

120 K. Zou, Z. Guan, Y. Deng and G. Chen, *Carbon*, 2020, **161**, 25–35.

121 S. Balou, S. E. Babak and A. Priye, *ACS Appl. Mater. Interfaces*, 2020, **12**, 42711–42722.

122 T. Varila, D. Bergna, R. Lahti, H. Romar, T. Hu and U. Lassi, *BioResources*, 2017, **12**, 8078–8092.

123 Z. G. Liu, Y. X. Huang and G. J. Zhao, *Bioresources*, 2016, **11**, 3178–3190.

124 S. Wu, P. Yan, W. Yang, J. Zhou, H. Wang, L. Che and P. Zhu, *Chemosphere*, 2021, **264**, 128557.

125 X. Liu, Y. Zhou, W. Zhou, L. Li, S. Huang and S. Chen, *Nanoscale*, 2015, **7**, 6136–6142.

126 J. Xu, B. Xue, C. Liu, C. Xia, M. Li and R. Xiao, *Sustainable Energy Fuels*, 2021, **5**, 3884–3894.

127 W. Liu, J. Yang, S. Liu, W. Yi, Y. Sun and G. Yang, *J. Energy Storage*, 2022, **46**, 103697.

128 M.-Y. Zhang, X.-J. Jin and Q. Zhao, *New Carbon Mater.*, 2014, **29**, 89–95.

129 M.-Y. Zhang, X.-J. Jin and Q. Zhao, *Carbon*, 2014, **76**, 471.

130 L. Yue, Q. Xia, L. Wang, L. Wang, H. DaCosta, J. Yang and X. Hu, *J. Colloid Interface Sci.*, 2018, **511**, 259–267.

131 M. Galhetas, A. S. Mestre, M. L. Pinto, I. Gulyurtlu, H. Lopes and A. P. Carvalho, *J. Colloid Interface Sci.*, 2014, **433**, 94–103.

132 I. I. Gurten, M. Ozmak, E. Yagmur and Z. Aktas, *Biomass Bioenergy*, 2012, **37**, 73–81.

133 J. Mi, X.-R. Wang, R.-J. Fan, W.-H. Qu and W.-C. Li, *Energy Fuels*, 2012, **26**, 5321–5329.

134 T. Tay, S. Ucar and S. Karagoz, *J. Hazard. Mater.*, 2009, **165**, 481–485.

135 W. Ruan, Y. Wang, C. Liu, D. Xu, P. Hu, Y. Ye, D. Wang, Y. Liu, Z. Zheng and D. Wang, *J. Anal. Appl. Pyrolysis*, 2022, **168**, 105710.

136 Z. Ma, Y. Zhang, C. Li, Y. Yang, W. Zhang, C. Zhao and S. Wang, *Bioresour. Technol.*, 2019, **292**, 122034.

137 F. Sun, J. Gao, Y. Yang, Y. Zhu, L. Wang, X. Pi, X. Liu, Z. Qu, S. Wu and Y. Qin, *Carbon*, 2016, **109**, 747–754.

138 W. Yu, F. Lian, G. Cui and Z. Liu, *Chemosphere*, 2018, **193**, 8–16.

139 Y. Ding, Y. Li, Y. Dai, X. Han, B. Xing, L. Zhu, K. Qiu and S. Wang, *Energy*, 2021, **216**, 119227.

140 C. H. Hsu, Z. B. Pan, H. T. Qu, C. R. Chen, H. P. Lin, I. W. Sun, C. Y. Huang and C. H. Li, *RSC Adv.*, 2021, **11**, 15738–15747.

141 X. Liu, S. Zuo, N. Cui and S. Wang, *Carbon*, 2022, **191**, 581–592.

142 S. Pérez-Rodríguez, D. Sebastián, C. Alegre, T. Tsoncheva, N. Petrov, D. Paneva and M. J. Lázaro, *Electrochim. Acta*, 2021, **387**, 138490.

143 L. Xiaorui, Y. Haiping, T. Yuanjun, Y. Chao, J. Hui and X. Peixuan, *Bioresour. Technol.*, 2024, **403**, 130865.

144 H. Liao, S. Fan, W. Han, M. Wang, Q. Shi, Y. Xie, X. Yang and W. Chen, *J. Energy Storage*, 2024, **100**, 113548.

145 L. Cheng, Y. Ji and X. Liu, *Chem. Eng. Sci.*, 2021, **233**, 116432.

146 L. Cheng, Y. Ji, X. Liu, L. Mu and J. Zhu, *Chem. Eng. Sci.*, 2021, **242**, 116739.

147 Y. Cheng, S. Zhao, H. Li, S. He, J.-P. Veder, B. Johannessen, J. Xiao, S. Lu, J. Pan, M. F. Chisholm, S.-Z. Yang, C. Liu, J. G. Chen and S. P. Jiang, *Appl. Catal., B*, 2019, **243**, 294–303.

148 X. Zhang, H. N. Tran, Y. Liu, C. Yang, T. Zhang, J. Guo, W. Zhu, M. Ahmad, H. Xiao and J. Song, *J. Cleaner Prod.*, 2023, **383**, 135527.

149 L. Ye, Y. Ying, D. Sun, Z. Zhang, L. Fei, Z. Wen, J. Qiao and H. Huang, *Angew Chem. Int. Ed. Engl.*, 2020, **59**, 3244–3251.

150 X. Wang, X. Li, S. Ding, Y. Chen, Y. Liu, M. Fang, G. Xiao and Y. Zhu, *Nano Energy*, 2021, **90**, 106541.

151 T. L. Dinadayalane, J. Lazare, N. F. Alzaaqi, D. Herath, B. Hill and A. E. Campbell, in *Theoretical and Computational Chemistry*, Elsevier, Amsterdam Netherlands, 2022, vol. 21, ch. 6, pp. 211–248.

152 C. Zhan, Y. Zhang, P. T. Cummings and D. E. Jiang, *Phys. Chem. Chem. Phys.*, 2016, **18**, 4668–4674.

153 M. Yang and Z. Zhou, *Adv. Sci.*, 2017, **4**, 1600408.

154 D. Adekoya, X. Gu, M. Rudge, W. Wen, C. Lai, M. Hankel and S. Zhang, *Adv. Funct. Mater.*, 2018, **28**, 1803972.

155 Y. Xu, C. Wang, P. Niu, Z. Li, L. Wei, G. Yao, F. Zheng and Q. Chen, *J. Mater. Chem. A*, 2021, **9**, 16150–16159.

156 Y. Xu, C. Zhang, M. Zhou, Q. Fu, C. Zhao, M. Wu and Y. Lei, *Nat. Commun.*, 2018, **9**, 1720.

157 X. Chang, X. Zhou, X. Ou, C. S. Lee, J. Zhou and Y. Tang, *Adv. Energy Mater.*, 2019, **9**, 1902672.

158 H. Li, M. Tang, X. Huang, L. Wang, Q. Liu and S. Lu, *Chem. Eng. J.*, 2023, **466**, 143095.